ELSEVIER

Journal of Fluids and Structures 22 (2006) 1057–1077

JOURNAL OF FLUIDS AND STRUCTURES

www.elsevier.com/locate/jfs

Normal forces on cylinders in near-axial flow

S. Ersdal*, O.M. Faltinsen

Centre for Ships and Ocean Structures, Norwegian University of Science and Technology, NO 7491 Trondheim, Norway

Received 13 September 2005; accepted 18 May 2006
Available online 29 September 2006

Abstract

The transverse forces on submerged cylinders in nearly axial flow were studied experimentally in a towing tank. Two rigid cylinders with length to diameter ratios of 10 and 30 were towed with angles from 0° to 20° between their centerline and the incoming flow, and with a combination of forced harmonic oscillations in the normal direction and constant speeds along the cylinder axis. The most important parameters are found to be the angle of attack and a Reynolds number combining the longitudinal and normal components of the flow. The Reynolds number is important because the transition from laminar to turbulent boundary layer due to the axial component of the flow has a significant influence on the normal force. This seems to be true both for constant and oscillating angle of attack. The finite length of the cylinder and the Keulegan–Carpenter number associated with an oscillating cylinder in cross-flow are found to be less influential than expected. Time-domain simulation models for the normal force suitable for general motion of the body are discussed. For constant angles of attack their standard deviation is found to be comparable to the measurement accuracy, but in the case of forced transverse oscillations the estimated errors of the force models increase to a factor three or more of the measurement errors.

Keywords: Hydrodynamic force; Oscillating cylinder; Angle of attack

1. Introduction

Knowledge of the normal force on a cylinder in near-axial flow is necessary in the analysis of marine system behavior such as the motion of towed sonar and hydrophone arrays, current loading on pipelines and marine risers, and maneuvering of slender underwater vehicles and even surface ships. This paper discusses the viscous hydrodynamic normal forces on a long cylinder of constant cross-section in infinite fluid when the angle of attack is small. The angle of attack is the angle between the ambient flow and the cylinder axis, and by small is meant that the angle is smaller than what is normally accepted as a valid region for the cross-flow principle. The angles discussed range from 0° to 20° in the case of a stationary cylinder, while the amplitude of the angle varies from 4° and up to 50° in the oscillating case. The normal force is defined as the force normal to the cylinder axis in the plane formed by the incident flow velocity vector and the cylinder axis. Such a force will include skin friction, but at some point the flow will separate on the leeward side of the cylinder and pressure forces similar to the drag of bluff bodies become significant and will have a component normal to the cylinder axis. If the flow is not symmetric about the plane of the cylinder axis and the incident flow, there

*Corresponding author. Tel.: +47 92 68 11 00.
E-mail address: svein.ersdal@akerkvaerner.com (S. Ersdal).

0889-9746/$ - see front matter © 2006 Published by Elsevier Ltd.
doi:10.1016/j.jfluidstructs.2006.05.003

will in addition be a bi-normal force component which is not presently considered. Also, the flow, and then the force, may develop along the cylinder so that a moment is created. For parts of a body where the cross-section changes, like nose and tail, there will also be a transverse force due to potential flow, usually found by slender body theory (Lighthill, 1960; Newman, 1977). These kinds of forces are not focused on here and care is taken to exclude them in the experimental set-up.

The normal force on a cylinder at constant angle of attack moving at constant speed relative to the ambient flow can be formulated in a general form suggested by Taylor (1952):

$$F_n = C_n(\alpha)\tfrac{1}{2}\rho V^2 Ld. \tag{1}$$

Here V is the relative velocity between the cylinder section and the ambient flow, ρ the density of the fluid, d the diameter and L the length of the section, and α the angle of attack. The normal force coefficient $C_n(\alpha)$ may for example be expressed in a polynomial expansion in the sine of the angle

$$C_n(\alpha) = C_{n1}\sin\alpha + C_{n2}\sin\alpha|\sin\alpha|, \tag{2}$$

where the absolute sign in the second term is used to preserve the sign of the resulting force. The normal force can also be expressed in terms of the normal component of the velocity v as

$$v = V\sin\alpha, \tag{3}$$

and Eq. (1) then becomes

$$F_n = C_{n1}\tfrac{1}{2}\rho VvLd + C_{n2}\tfrac{1}{2}\rho v|v|Ld. \tag{4}$$

Note that the coefficients are the same in both formulations.

In studies of the transverse stability of towed arrays, only small transverse motions are considered and the angle of attack (α) is usually assumed small enough for the flow not to separate (Dowling, 1988; Triantafyllou and Chryssostomidis, 1988). Then the normal force is expressed as the normal component of the skin friction, here obtained by setting the coefficients in Eq. (2) to

$$\begin{aligned} C_{n1} &= \pi C_F, \\ C_{n2} &= 0. \end{aligned} \tag{5}$$

The coefficient C_F is the skin friction coefficient for $\alpha = 0$ and the factor π is included for a circular cylinder, since Eq. (1) is normalized by the diameter times the length rather than the wetted surface. For small amplitudes and low frequencies of the transverse motion, the relative velocity V is approximately equal to the tow-speed U of the array and may therefore be considered a constant. Inserting this in Eq. (4) gives that the resulting expression for F_n is linear with the normal component of the incident flow, facilitating a linear equation of motion for the towed array. A throughout discussion of this equation and alternative values of C_{n1} is given by Païdoussis (2004).

For high angles, the normal force is usually expressed by the drag of a cross-section of the body when exposed to the normal component of the velocity, v; see, e.g., Faltinsen (1990, Chapter 7). This is denoted as the cross-flow principle and may be expressed by setting

$$\begin{aligned} C_{n1} &= 0, \\ C_{n2} &= C_d. \end{aligned} \tag{6}$$

Here C_d is the mean drag coefficient for steady-state flow past a 2-D section. This assumes that the flow pattern along the leeward side of the cylinder corresponds to a fully developed wake behind a cross-section and implicitly that the angle of attack is close to 90°. The range of allowed angles is a matter of comparison with experiments, and are often said to be above 45° (Faltinsen, 1990). For 2-D steady flow past a cylinder in infinite fluid it is well known that the value of the drag coefficient changes with Reynolds number of the flow, roughness of the cylinder surface, and the turbulence intensity of the incident flow (Faltinsen 1990, Chapter 6). There is a sub-critical region where the boundary layer flow is laminar up until the separation point and a transcritical region where the flow becomes turbulent well before the separation point. Typical values for a smooth cylinder and low turbulence of the incoming flow are $C_d = 1.2$ for sub-critical region and $C_d = 0.8$ for the transcritical region (Blevins, 1992, Table 10.18). There is also a critical region between the two where the drag coefficient changes rapidly with Reynolds number and may become even lower than in the transcritical region. For low angles the boundary layer may be turbulent due to the tangential component of the flow, and the effect of this on the normal force is discussed in Section 3.

The 2D + t principle described by Faltinsen (2005) accounts for the fact that the flow pattern associated with the cross-flow model may not have time to develop along a finite length cylinder due to the axial component of the incident

flow. Consider an Earth-fixed plane perpendicular to the axis of the body. As the body pierces the plane, its trace moves laterally in the plane with a velocity v. The flow in the plane is then assumed 2-D but time dependent and similar to the impulsive start of a cylinder (Jorgensen and Perkins, 1958; Bryson, 1959). This is expressed in the form of Eq. (2) by averaging the drag coefficient along the cylinder in the second term:

$$C_{n1} = 0,$$
$$C_{n2} = \overline{C_D} = \frac{1}{L}\int_{x_0}^{x_L} C_d(x,\alpha)\,\mathrm{d}x, \tag{7}$$

where x_0 and x_L correspond to the position where separation starts and the aft end of the cylinder, respectively. $C_d(x,\alpha)$ is the time-dependent drag coefficient of an impulsively started cylinder cross-section mapped along the length of the test-section, setting $x = x_0 + Vt\cos\alpha t$. The time t is zero at the time of the impulsive start in the 2-D case. Here it is assumed that separation starts at the transition from the nose (with expanding cross-section) to the part of the body with constant cross-section, as concluded by Jorgensen and Perkins (1958). The normal force on the part of the body in front of the separation point is not included in this analysis. The force history of an impulsively started cylinder is approximated by a fifth-order polynomial fit to experimental results by Sarpkaya (1966); see Faltinsen (2005). This is the solid line in Fig. 1. This mapping implicitly assumes laminar boundary layer flow, and since there will always be a finite acceleration in experiments a true impulsive start cannot be obtained. Both effects are likely to influence the time history, see for example Sarpkaya's result with a turbulent boundary layer where a constant value of C_d was reached almost instantly (Sarpkaya, 1966). Therefore, an alternative time history is given by the dashed line in Fig. 1, where the fifth-order polynomial is scaled so that the peak coincides with the peak time found numerically by Koumoutsakos and Leonard (1995), also for laminar boundary layers. Averaged drag coefficients based on the original curve fit are shown in Fig. 2(a), while drag coefficients based on the scaled curve fit are shown in Fig. 2(b). As shown in Fig. 2, the $2D+t$ model will generally give smaller normal forces than the cross-flow principle for the same cylinder and angle. Unfortunately, the actual value depends highly on the time history of the 2-D drag coefficient, so a quantitative value will be somewhat uncertain.

In cases where the acceleration of the cylinder is not zero, the hydrodynamic force will depend not only on the velocity but also on the acceleration. In the current case the ambient fluid is at rest, so only the acceleration of the body is considered. The so-called Froude–Kriloff force, or the force due to the ambient fluid pressure, is zero. For periodic motion it will be assumed that the normal force is also periodic, so it can be expressed in a Fourier series of a normal force coefficient D_n which includes also the effect of acceleration:

$$F_n(t) = -D_n(\theta)\tfrac{1}{2}\rho u^2\, Ld, \tag{8}$$

$$D_n(\theta) = A_0 + \sum_{k=1}^{\infty}(A_k \sin k\theta + B_k \cos k\theta), \tag{9}$$

where $\theta = \omega t$, ω is the circular frequency of the forced oscillation and u is the incident velocity along the cylinder axis. The use of u to normalize the force is based on the set-up of the experiment, since this is the tow-speed of the carriage. The transverse motion of the cylinder is symmetric about the mean horizontal position and, assuming that this is the case also for the normal force, $A_0 = 0$ and only odd values of k need to be included in the series. The coefficients can then be estimated from the measurements by

$$A_k = \frac{1}{\pi}\int_{\theta=0}^{2\pi} D_n(t)\,\sin k\theta\,\mathrm{d}t, \tag{10}$$

$$B_k = \frac{1}{\pi}\int_{\theta=0}^{2\pi} D_n(t)\,\cos k\theta\,\mathrm{d}t, \tag{11}$$

valid for $k \geq 1$. Here $D_n(t)$ is the measured force coefficient. The assumptions here are the same as used by Keulegan and Carpenter (1958), and nothing in the current experiments seems to contradict them.

Alternatively, the force may be expressed as the sum of terms depending on the acceleration and velocity of the cylinder:

$$F_n = -C_a\rho\frac{\pi d^2}{4}L\dot{v} - C_n(\alpha)\frac{1}{2}\rho V^2 Ld, \tag{12}$$

where C_a is the added mass coefficient and $\dot{v}$ is the time derivative of the normal velocity v. The term associated with $\dot{v}$ will in the following be denoted the inertia term. The velocity-dependent term in Eq. (12) will be termed the drag part, and is here expressed in the same way as for the stationary cylinder in Eq. (1), with a relative velocity $V = \sqrt{u^2+v^2}$.

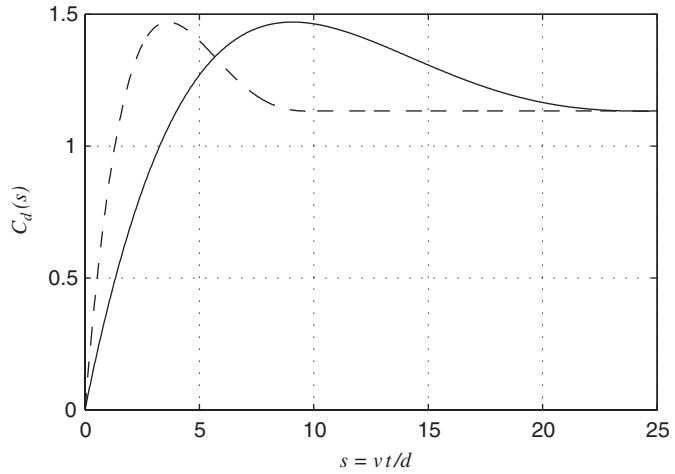

Fig. 1. Drag coefficient of impulsively started cylinder section with laminar boundary layer: —, curve fit of experimental data from Sarpkaya (1966); – –, curve fit scaled so peak coincide with numerical results of Koumoutsakos and Leonard (1995).

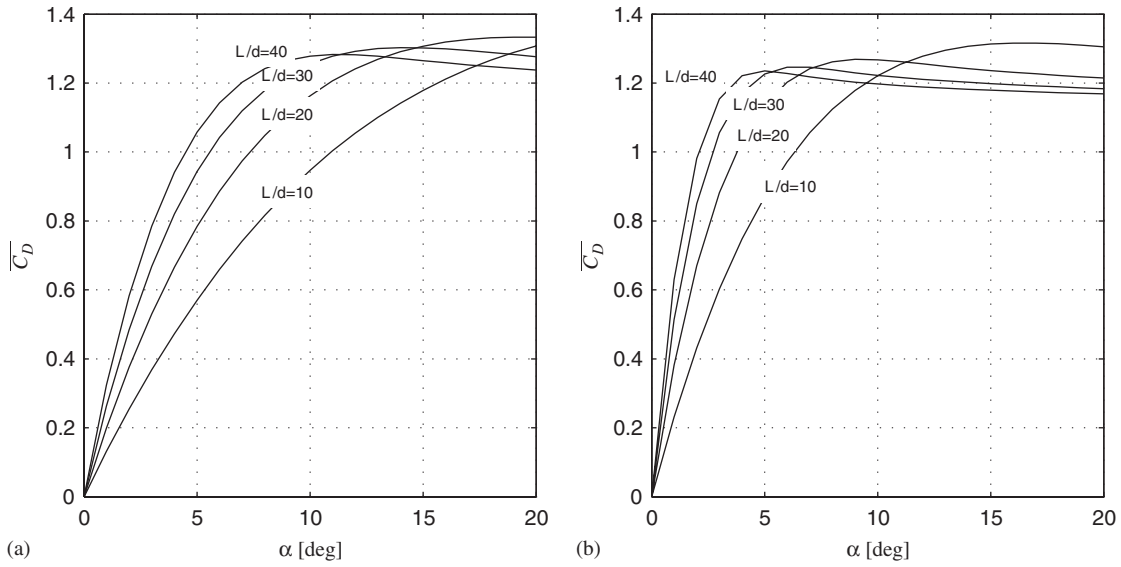

Fig. 2. Averaged drag coefficients as function of the angle of attack according to $2D + t$ theory: (a) based on the solid line in Fig. 1; (b) based on the dashed line in Fig. 1.

In general, the coefficients C_a and C_n are not constant but depend on the history of the motion (Keulegan and Carpenter, 1958).

Using the velocity-based formulation of the normal force in Eq. (4) and the cross-flow principle with coefficients as in Eqs. (6), (12) becomes

$$F_n = -C_a\rho\frac{\pi d^2}{4}L\dot{v} - C_d\frac{1}{2}\rho v|v|Ld \tag{13}$$

which is similar to Morison's equation but valid for a cylinder oscillating in a fluid at rest.

Forcing the coefficients C_a and C_d in Eq. (13) to be constant, they can be directly related to the leading terms of the Fourier series of $C_n(\theta)$ by a procedure described by Keulegan and Carpenter (1958). The transverse oscillation is

described by $y = A \sin\theta$, so the transverse velocity and acceleration is

$$v = \omega A \cos\theta, \tag{14}$$

$$\dot{v} = -\omega^2 A \sin\theta. \tag{15}$$

Inserting this in Eq. (12) and comparing with the Fourier series in Eqs. (8) and (9) the added mass coefficient is

$$C_a = -\frac{2}{\pi}\frac{A}{d}\left(\frac{\omega A}{u}\right)^{-2} A_1. \tag{16}$$

The series expansion of the quadratic velocity term in Eq. (13) is (Keulegan and Carpenter, 1958)

$$(\omega A)^2 \cos\theta|\cos\theta| \simeq (\omega A)^2\left(\frac{8}{3\pi}\cos\theta + \frac{8}{15\pi}\cos 3\theta + \cdots\right). \tag{17}$$

Comparing this to the drag part of Eq. (13) gives in leading order of $\cos\theta$

$$C_d = \frac{3\pi}{8}\left(\frac{\omega A}{u}\right)^{-2} B_1. \tag{18}$$

If the leading order term of the cosine part of the Fourier series is compared to the drag term in Eq. (12), the normal force coefficient can be expressed by

$$C_n(\alpha) = B_1\left(\frac{\omega A}{u}\right)^{-1} \cos\alpha \sin\alpha, \tag{19}$$

where the coefficient is constant in time but varies with oscillation amplitude.

Note that all these expressions include the first terms of the Fourier series only, so that Eq. (12) with constant coefficients is only a first-order approximation to the complete normal force.

2. Measurement procedure and accuracy

The normal forces on two cylinders of length 1.5 and 0.5 m were measured when towed with constant carriage speed either at a constant angle of attack or with a harmonic oscillation in the normal direction. The main parameters of the experiment are given in Table 1.

The actual set-up is shown in Fig. 3 with the Cartesian coordinate system (x, y, z) indicated. This is a body-fixed system with x-axis along the cylinder axis positive in the tow direction when $\alpha = 0$ and with the z-axis pointing upwards. For all the tests performed here, the plane of the normal force corresponds to the x–y plane in Fig. 3. The nose was made of polycarbonate and was parabolic in shape. The test-sections were spray-painted thin-walled steel pipes with plugs at each end, so the cylinders were dry inside. The aft support structure was also made of steel, with details of aluminum. The complete set-up was mounted on the towing carriage in the Marine Cybernetics Laboratory at the Marine Technology Center, NTNU. This basin is 30 m long, 6 m wide and 1.5 m deep; see Fig. 4. The carriage allows forced motions of a model in five degrees of freedom. The tow depth of the cylinder axis was 540 mm, or about 11 diameters. Load cells of type HBM PWSM-10 were placed between the nose and the test-section and between the test-section and the aft support structure. These cells measured the shear force in the y-direction indicated in Fig. 3 and was connected to a HBM MGC+ amplifier and D/A converter unit. The position of the carriage at all times was also recorded by this unit based on encoder output from the carriage motors. All signals were recorded at 100 Hz and filtered at 20 Hz before storage on disk. Final signal analysis was done on a PC using the MATLAB package from MathWorks Inc.

For constant angles, the set-up was rotated about the z-axis in Fig. 3, while the forced oscillation was performed in the y-direction. In all cases the cylinder was towed with constant speed in the direction coinciding with the x-axis when $\alpha = 0$. The orientation and motion of the test-section were described as inputs to the carriage control system. To ensure that the orientation of the cylinder was correct, angles on both sides of the assumed zero angle position were tested and checked before the tests involving forced oscillations were performed.

The time between each run was at least 10 min in order to allow waves and wakes to dissipate. The forces were measured from before the carriage started to move and until it had come to a complete stop, while the results presented here are based on the steady-state part of the recordings. The normal force on the test-section was taken as the

Table 1
Parameters for the experiment

Length-to-diameter ratio	$L/d = 31.25$ and 10.46
Masses: nose section	0.255 kg
Long test cylinder	4.480 kg
Short test cylinder	1.780 kg
Reynolds numbers	$\mathrm{Re}_L = 0.19 - 2.0 \times 10^6$
Tow-speed	$U = 0.4$–$1.4\,\mathrm{m\,s^{-1}}$
Diameter	$d = 0.048\,\mathrm{m}$
Roughness-to-diameter ratio	$k/d \simeq 3 \times 10^{-5}$
Water density	$\rho = 998.5\,\mathrm{kgm^{-3}}$
Dynamic viscosity	$v = 1.05 \times 10^{-6}\,\mathrm{m^2\,s^{-1}}$
Constant angles of attack	$\alpha = -5^\circ$ to $+20^\circ$
Oscillation amplitude-to-diameter ratios	$A/d = 1$, 2, and 3
Oscillation frequency range	0.127–0.547 Hz

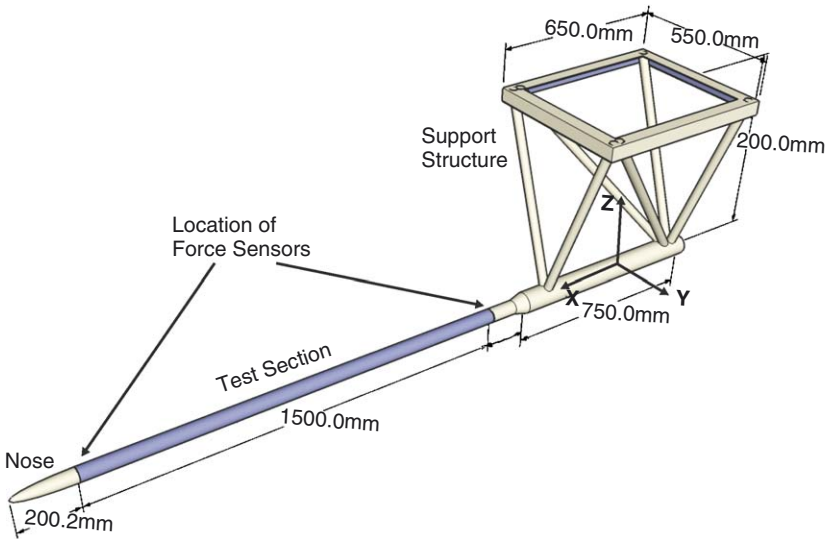

Fig. 3. Experimental set-up for transverse forces on a submerged, rigid cylinder, here with the long test-section. Rotation was performed about the z-axis indicated and oscillation along the y-axis.

difference between the force measurements in each end of the section. In the case of forced oscillations, the inertia forces due to the mass of the test-section as listed in Table 1 were subtracted before any analysis was performed.

The accuracy of the results will be expressed by the 95% confidence interval as outlined in ITTC (1990) and Coleman and Steele (1989), with both precision and bias errors included. It is then expected that for repeated measurements of some coefficient C, Eq. (20) is true for 95% of the results:

$$C \in C_0 \pm e_c, \tag{20}$$

$$e_c = \sqrt{\left(t_{95}\frac{S_m}{\sqrt{N}}\right)^2 + \beta_m^2}. \tag{21}$$

Here C_0 is the estimated value obtained from measurements and e_c describes the width of the error band with a specified confidence. S_m is the standard deviation of N repeated measurements and the factor t_{95} corresponds to a 95%

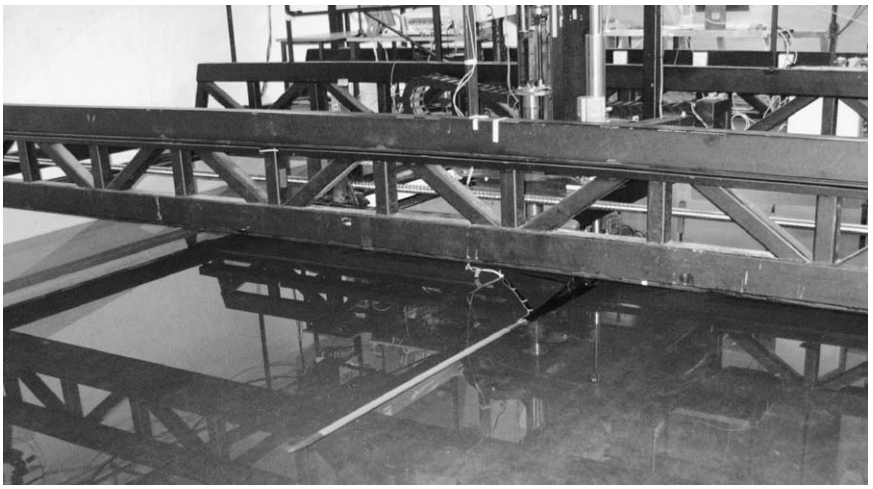

Fig. 4. Experimental set-up mounted in the Marine Cybernetics Laboratory.

Table 2
Estimated error levels for constant angle of attack

Angle of attack		0°–6°	6°–12°	>12°
Standard deviation of measured force (N)	S_m	0.01	0.03	0.06
Error in calibration factor (N)	β_1	0.25×10^{-3}	1.0×10^{-3}	5.0×10^{-3}
Max deviation of angle of attack (degrees)	β_3	0.01	0.05	0.15
Max error in tow-speed ($\mathrm{m\,s^{-1}}$)	β_4		3.5×10^{-3}	
Others (N)	β_5		$0.1\,S_m$	
Bias error, Eq. (22)	β_m	4.0×10^{-5}	2.6×10^{-4}	2.0×10^{-3}
Total error, Eq. (21)	e_c	0.7×10^{-3}	2.1×10^{-3}	4.6×10^{-3}

confidence interval using the Student's t distribution with $N-1$ degrees of freedom. For a constant angle, S_m was estimated by repeating selected runs six or more times. For the oscillating case, all parameter estimations were done for a single period, and the S_m value represents the standard deviation from period to period. The lowest number of periods used in the analysis is 4 for the cases that combine highest speed and lowest frequency, while in most cases 12 or more periods are included.

Known bias errors, such as the true angle of zero force, were corrected for in the analysis of the results. Still, there will be some uncertainties that will not vary when repeating the experiments, given by β_m in Eq. (21). They are calculated from

$$\beta_m = \sum_{i=1}^{i=M} \sqrt{\kappa_i^2 \beta_i^2}, \tag{22}$$

$$\kappa_i = \frac{\partial C}{\partial X_i}. \tag{23}$$

Here β_i is the bias uncertainty of parameter X_i, and κ_i represents the effect of this error on the result, usually known as the sensitivity. Identified bias errors and their estimated values are given in Table 2.

The main challenge of designing and building the experimental set-up was to ensure sufficient rigidity of the structure. All position measurements are related to the support structure, so any flexibility in the structure will not be captured. The use of a steel pipe ensured rigidity of the test-section, while the aft support and load cell assembly represented the

main challenge, particularly since some flexibility is necessary when using load cells based on strain gages. The maximum deviation of the angle given in Table 2 was found by measuring the deflection due to a known weight and then relate this to the maximum measured forces in the given range of angles. The sensitivity κ was found by local linearization of the measured results in Fig. 6.

Some vibrations of the test-section must be expected when mounted on a motor-driven carriage. The lowest eigenfrequency of the set-up was estimated by modelling the sensor as a rotational spring and the test-section as a rigid beam. The spring constant of this spring was found by measuring the static deflection of the forward end of the test-section when subjected to a known, static load. The value from a linear square fit of the measurements corresponded well with stiffness specification given for the sensor. The result for the long cylinder was an eigenfrequency of 4.6 Hz, which was confirmed by performing fast Fourier transforms (FFT) on the measured time series. By reading the force sensor outputs for known loads and deflections, the relation between the measured force and the deflection of the test-section front end was established. The standard deviation of the force measurement within a single run was at worst 1 N, which corresponds to a peak-to-peak amplitude of 1.1 mm at the forward end. This amplitude is small compared to the diameter and even if the mass transport described by Schlichting (1979) for a 2-D cylindrical cross-section oscillating with small amplitude and laminar boundary layer flow takes place, there should be no effect on the mean value of the force. The effect of vibration is therefore included in the precision error and not as a bias uncertainty. The same assumption is used in the oscillating case where the time series are filtered by a forward and inverse FFT procedure at a frequency slightly below the lowest eigenfrequency.

Calibration was performed at the same time as the deflection studies, recording the voltage outputs with known loading. The estimated calibration errors were found from the variation of the factor when calculating it from different measurements.

The uncertainty of the tow speed was estimated by comparing the derivative of the measured position of the carriage with the speed setting in the input.

The *other* category in Table 2 includes effects like clearances at the test-section ends, cylinder vibrations, generated waves, residual flow in the tank, and model dimensions. A comprehensive discussion of these effects is given in Ersdal (2004), where the residual wake flow in the tank was found to be the most important. The combined effect was found be no more than 10% of the precision error of the force measurement, so this number is used here. In the experiments described in Ersdal (2004) a pair of struts was placed also in front of the test-section. The presence of these struts was found to give significant bias errors, thus the cantilever beam design of the present set-up. Other error sources like sensor errors, alignment, and errors in the analysis procedure are assumed to be precision errors only, and therefore accounted for by repeating the experiments. Care was taken in analyzing the experiments to avoid systematic errors due to filtering and time series end-effects.

In order to ensure a turbulent boundary layer over the length over the cylinder for $\alpha = 0$, a band of silica grains was applied around the aft part of the nose, see Fig. 5(a). For the cylinder diameter and Reynolds numbers involved here, there is no effect of curvature in the friction coefficient according to White (1972), thus the boundary layer is assumed to be that of a flat plate. The required roughness height to trip the boundary layer to turbulent state is then $\varepsilon > 820\nu/U$ (Blevins, 1992), where ν is the kinematic viscosity of the fluid. For a tow speed $U = 0.4\,\mathrm{m\,s^{-1}}$ this requires the roughness height, or grain size, of 2 mm. For comparison, a screen was placed upstream of the cylinder as shown in Fig. 5(b) to ensure a turbulent boundary layer at all angles for selected runs. The screen consisted of a wire mesh with wire diameter 2 mm and a mesh size of 20 mm and was placed 250 mm upstream of the start of the test-section (the distance was kept constant as the angle of attack increased). Simplifying and considering a single bar element of the mesh, the turbulence level should be $\frac{1}{3}\sqrt{(u'^2 + v'^2 + w'^2)/(U^2)} \simeq 0.02$ at the start of the test-section, see in Blevins (1992, Appendix B). From Tables 10 and 11 in the same reference, boundary layer transition should then be completed at a Reynolds number $\mathrm{Re}_x \simeq 1 \times 10^5$. This number is slightly above the lowest Reynolds number at $x = 0.2$ m and $\alpha = 0$, but at least for tow-speed $U = 0.6\,\mathrm{m\,s^{-1}}$ the screen should ensure a turbulent boundary layer on the cylinder also for high angles.

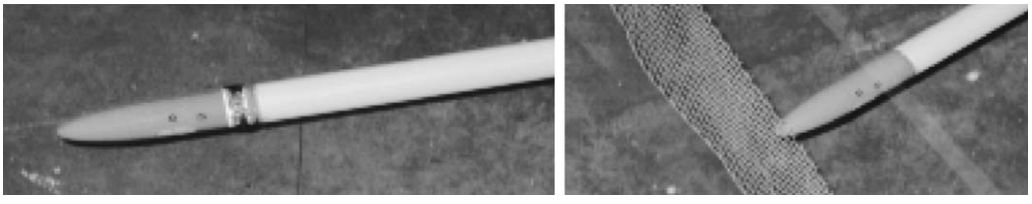

Fig. 5. Tripping the boundary layer: (a) silica grains applied in a band around the nose; (b) screen placed upstream of the cylinder.

The test-section is assumed to be smooth, which requires a roughness height $\varepsilon < 100v/U$ (Blevins, 1992, Tables 10–13). For relevant Reynolds numbers, this gives $k/d < 1.5 \times 10^{-3}$, which according to Table 1 is fulfilled for the spray-painted surface.

In the case of constant angles, the resulting transverse forces are represented as a nondimensional coefficient given by Eq. (1):

$$C_n = \frac{F_n}{\frac{1}{2}\rho V^2 L d}, \tag{24}$$

where F_n is the measured normal force on the test section, V the relative velocity between the body and the ambient fluid and d and L the diameter and length of the test-section as given in Table 1. In this case the carriage speed U equals the relative velocity so that $U = V$. The last two lines in Table 2 give the estimated bias and total error for this coefficient. The results in the last line are 5% or less of the measured values.

An alternative to Eq. (24) is to use Eq. (4) to form a coefficient related to the drag coefficient of a 2-D cross-section of the cylinder. However, because the normal component of the velocity defined in Eq. (3) will go to zero as $\alpha \to 0$, this representation of the results is very sensitive to errors in the angle of attack, and large scatter for small angles must be expected when representing the results this way.

For the oscillating cylinder the normal force is normalized with the velocity component along the axis u, see Eqs. (8) and (9). In the experiment the velocity is the tow-speed of the carriage, thus $u = U$ and the bias error estimates are the same as for the constant angle case. The alternative to u is the amplitude of the cross-flow velocity, but the problem of sensitivity for small values would then be the same as in the stationary case.

3. Measured forces at constant angle of attack

In Figs. 6–10 the measured normal force coefficients defined in Eq. (24) are plotted as a function of the angles of attack α. The gray areas in the plots represents the expected values based on the cross-flow principle, see Eq. (6). The area indicates values of C_d from 0.8 to 1.2, the expected values from Blevins (1992, Table 10.18).

Figs. 6 and 7 show the measured C_n values for the long cylinder at three different tow-speeds, Fig. 7 for small angles of attack. The boundary layer was in these cases tripped by the band of silica grains around the nose. For angles up to about 6°, the effect of changes in Reynolds numbers is small, while in the range from $\alpha \simeq 6°$ to 16° the effect is important. For even higher angles the Reynolds number dependence again seems to be small.

The range of C_d values in the 2-D case was explained by the state of the boundary layer, and something similar seems to take place here, but related to the Reynolds number of the longitudinal component of the flow. This is illustrated in Fig. 9 where the transverse drag coefficient is expressed as $C_d = C_n(\sin\alpha)^{-2}$. The argument of Fig. 9 is a Reynolds number based on the length parallel to the incident flow; $d\ (\sin\alpha)^{-1}$, here denoted the 'real' Reynolds number, see Fig. 8. The results in Fig. 9 are for all test cases with $\alpha > 4°$, including the short cylinder. As mentioned in the error analysis, some scatter must be expected due to the sensitivity of the angle of attack, but there definitely seems to be a transition region between $Ud/(v \sin\alpha) \simeq 2 \times 10^5$ and 3.5×10^5, which corresponds closely to the transition region for the 2-D case ($\alpha = 90°$); see, e.g., Faltinsen (1990, Chapter 6). For 'real' Reynolds number below this, which corresponds to high angles of attack, the flow is sub-critical according to the 2-D nomenclature, with an expected $C_d \simeq 1.2$. As the angle decreases, and/or the velocity increases, the 'real' Reynolds number increases (as does the scatter) and the flow becomes critical and eventually transcritical where $C_d \simeq 0.8$ is expected. This suggests some similarity of the current case and the drag reduction found in 2-D when a proper Reynolds number is applied.

To further investigate the effect of the boundary layer transition, Fig. 10 compares the results for the tripped boundary layer with measurements for the cylinder without the band of grains both in free stream and with a screen placed upstream as shown in Fig. 5(b). The results for the smooth cylinder follow the expected results for a laminar boundary layer, while results with the screen applied follow the expected results for a turbulent boundary layer, as expected from the above discussion.

Fig. 11 compares results with two different lengths of the cylinder. From the $2D + t$ results in Section 1 it is expected that the normal force coefficient on the short cylinder is smaller than for the long one when towed at the same velocity, particularly for angles of attack less than 5°. The experimental results show very little difference between the two cylinders, indicating that the steady flow pattern develops even more rapidly than suggested in Fig. 1. For the small angles, the boundary layer is turbulent for both cylinders in Fig. 11, so this compares with the conclusion of Sarpkaya (1966) that in turbulent flow the steady flow develops almost instantly. For angles above 10° the boundary layer may be

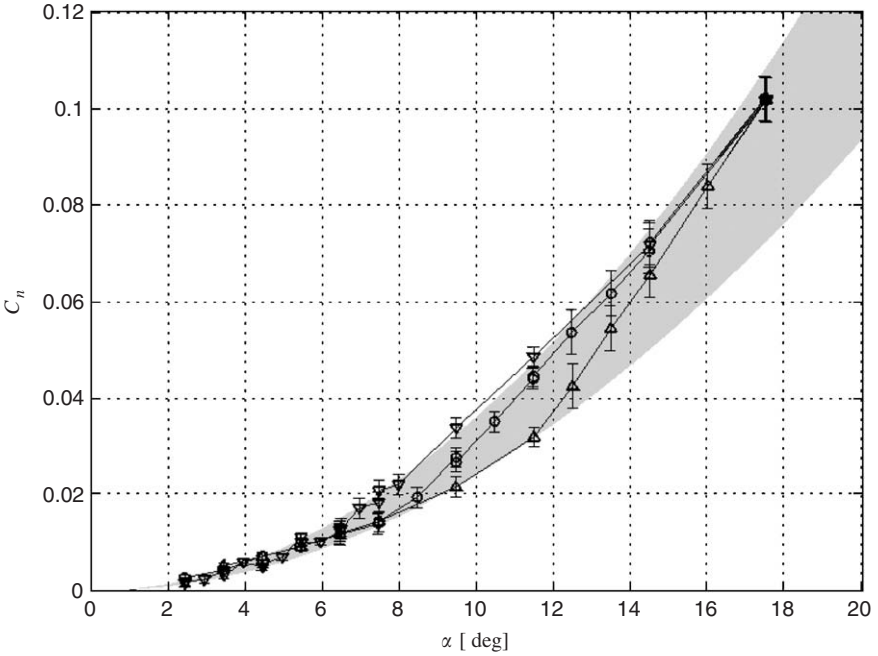

Fig. 6. Normal force coefficient at constant angles of attack α: ∇, $\mathrm{Re}_L = 0.86 \times 10^6$; $\circ$, $\mathrm{Re}_L = 1.4 \times 10^6$; $\triangle$, $\mathrm{Re}_L = 2.0 \times 10^6$, where $\mathrm{Re}_L = UL/v$. Bars represent 95% confidence interval and the gray area corresponds to expected range of values from the cross-flow principle.

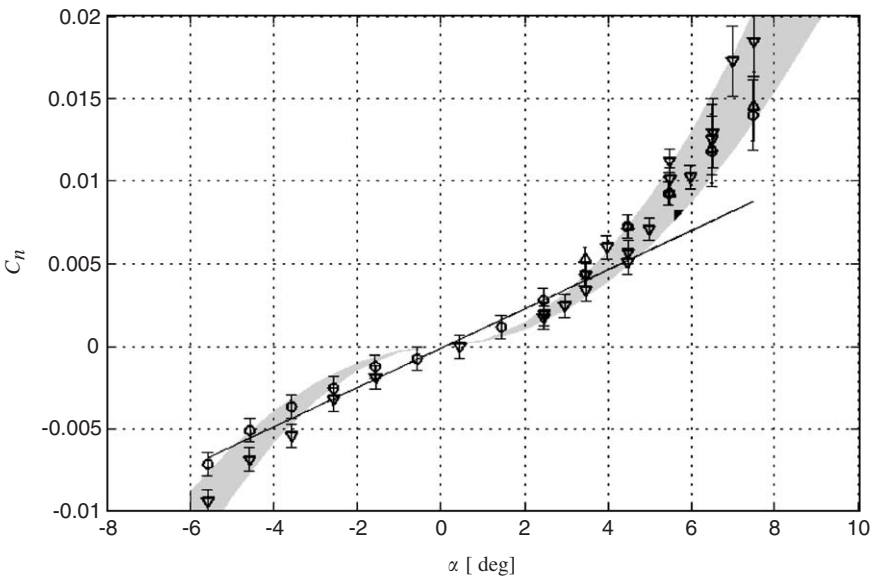

Fig. 7. Normal force coefficient (Eq. (24)) at angle of attack α close to zero: ∇, $\mathrm{Re}_L = 0.86 \times 10^6$; $\circ$, $\mathrm{Re}_L = 1.4 \times 10^6$; $\triangle$, $\mathrm{Re}_L = 2.0 \times 10^6$, where $\mathrm{Re}_L = UL/v$. Bars represent 95% confidence interval. The gray area corresponds to expected range of values from cross-flow principle while the solid line represent the linear model for $|\alpha| < 4^\circ$ with $C_{n1} = 0.068$.

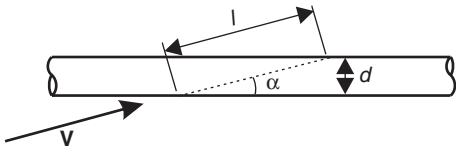

Fig. 8. The length l used in the 'real' Reynolds number.

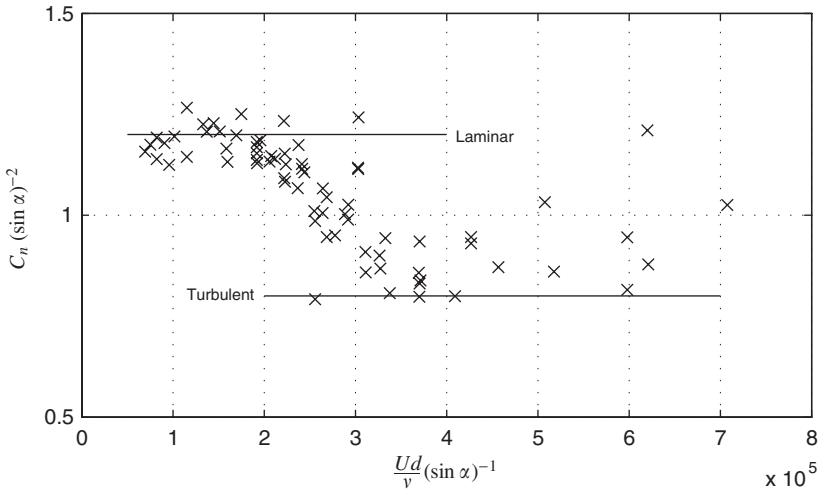

Fig. 9. Cross-flow drag coefficient as function of 'real' Reynolds number: —, expected values for a 2-D cylinder section with laminar and turbulent boundary layer at separation.

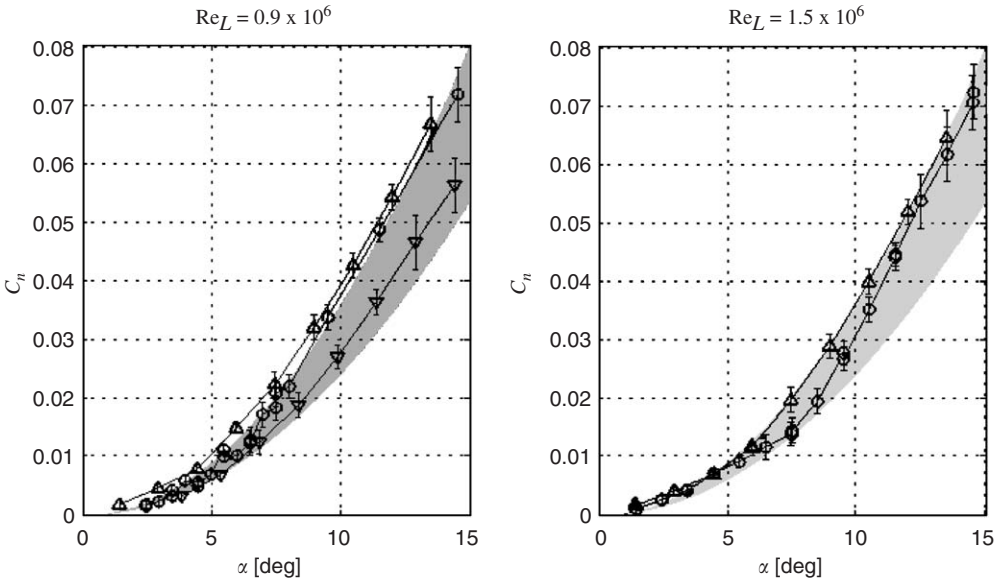

Fig. 10. Effect of boundary layer: ○, band of silica grains; △, smooth; ▽, upstream screen. Bars represent 95% confidence interval and the gray area corresponds to expected range of values from cross-flow principle.

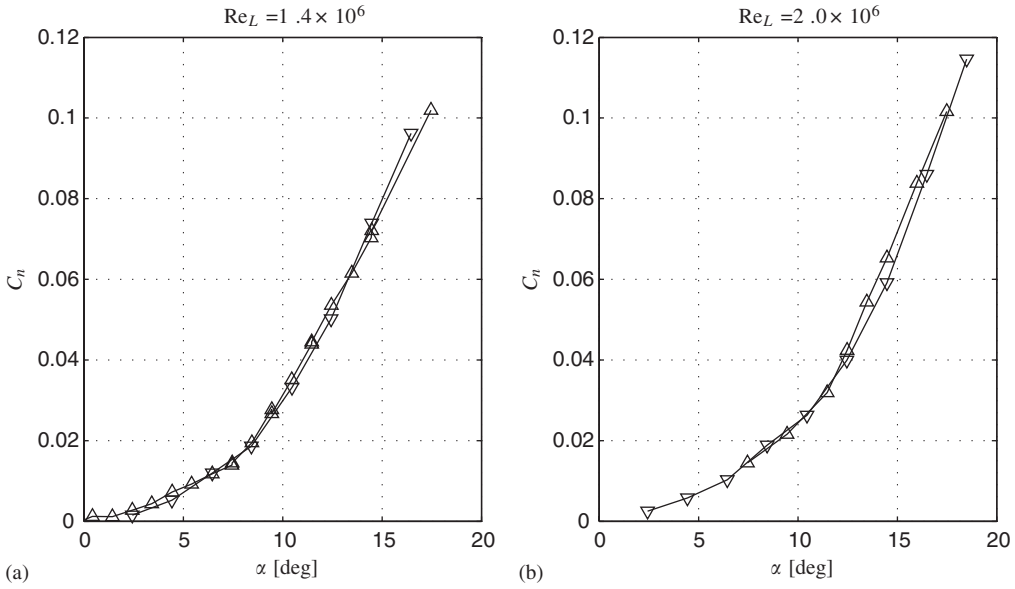

Fig. 11. Normal force coefficients for two cylinder length to diameter ratios when towed at the same velocity: ▽, $L/d \simeq 10$; △$L/d \simeq 30$. Reynolds numbers $\mathrm{Re}_L = UL/v$ refer to the long cylinder.

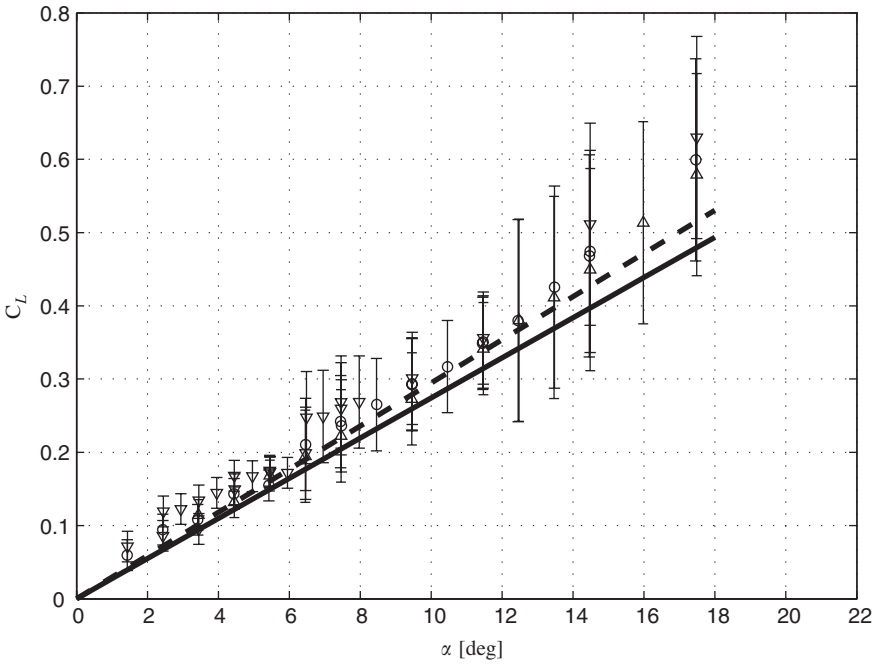

Fig. 12. Lift coefficient of the nose: ▽, $\mathrm{Re}_L = 0.84 \times 10^6$; ○, $\mathrm{Re}_L = 1.4 \times 10^6$; △, $\mathrm{Re}_L = 2.0 \times 10^6$, where $\mathrm{Re}_L = UL/v$; —, result from slender body theory; – –, correction for viscous effects. Bars represent 95% confidence interval.

laminar when the separation starts, but according to Fig. 2(b) the averaged force coefficient is close to the 2-D value at these angles and the effect of finite length of the cylinder is small also in this region.

The normal force on the nose section is not the focus here; but since the data is so readily available, the measured forces are compared to the slender body theory (Newman, 1977) in Fig. 12. The lift coefficient is

calculated from

$$C_L = \frac{F_{\text{nose}}}{\frac{1}{2}\rho U^2 d^2}, \tag{25}$$

where F_{nose} is the measured transverse force on the nose section. For small angles, slender body theory gives $C_L = \frac{1}{2}\pi\alpha$, with α in radians. A correction of 7.5% due to the viscous boundary layer was found in Hoerner and Borst (1985, Figs. 19 and 16) and is represented by the dashed line in Fig. 12. For most of the data points the expected values are within the error band of the measurements. The exceptions are for the lowest speed where the measured force seems to be a little higher than expected, and for $\alpha > 10°$–$12°$. In this range the angle of attack cannot be considered small, so some deviation must be expected.

4. Models of the normal force at constant angle of attack

Mathematical models of the normal force were discussed in the introduction. To compare models with the experiments in a systematic way, the standard error of estimation (SEE) will be used. This is defined as (Coleman and Steele, 1989)

$$\text{SEE} = \sqrt{\frac{1}{N-2}\sum_{i=1}^{N}(X_i^{\text{mod}} - X_i^{\text{exp}})^2}, \tag{26}$$

where X_i^{mod} and X_i^{exp} are the N modelled and experimentally measured values, respectively. By comparing this value to the experimental uncertainty, the "goodness" of a model can be expressed. If the error of estimation is less or equal to the experimental results the model is as good as the measurement and further improvement of the model is not possible based on the current data. Results for force models for constant angles of attack are given in Table 3. The first three models are discussed in the Introduction, see Eqs. (5)–(7). The coefficient in the cross-flow formulation is set to $C_d = 1.15$ rather than 1.2 since the lower value was found to minimize the estimation error. The last model is a modified version of the cross-flow principle to account for the change in coefficient due to the boundary layer. The normal force coefficient is then expressed

$$C_n = [C_{nt} + f(\alpha, U)(C_{nl} - C_{nt})] \sin\alpha|\sin\alpha|, \tag{27}$$

where C_{nl} and C_{nt} are the coefficients corresponding to laminar and turbulent boundary layer, respectively. The function $f(\alpha, U)$ varies between zero and one. From inspection of the experimental results in Fig. 6 it is chosen as a linear transition

$$f(\alpha, U) = \begin{cases} 0 & \text{if } \alpha < \alpha_t, \\ \dfrac{\alpha - \alpha_t}{\alpha_l - \alpha_t} & \text{if } \alpha_t \leqslant \alpha \leqslant \alpha_l, \\ 1 & \text{if } \alpha > \alpha_l. \end{cases} \tag{28}$$

The angle α_t is the upper limit for turbulent boundary layer and α_l is the lower limit for laminar boundary layer. The values are found from $Ud/v(\sin\alpha_t)^{-1} = 3.4 \times 10^5$ and $Ud/v(\sin\alpha_l)^{-1} = 2.0 \times 10^5$. The values of the coefficients in Eq. (27) are $C_{nt} = 0.8$ and $C_{nl} = C_d = 1.15$.

The modified cross-flow principle is then able to reproduce the results to the same accuracy as the measurements and can therefore be judged as a success. The exception is angles less than $4°$–$5°$ where a linear model performs slightly

Table 3
Suggested models for constant angle of attack

Case	C_n	SEE	$\overline{e_c}$
Linear ($\lvert\alpha\rvert <= 4°$)	$0.068 \sin\alpha$	1.25×10^{-3}	0.70×10^{-3}
Cross-flow principle	$1.15 \sin\alpha\lvert\sin\alpha\rvert$	3.77×10^{-3}	2.17×10^{-3}
2D + t with laminar boundary layer	$\overline{C_D} \sin\alpha\lvert\sin\alpha\rvert$	8.42×10^{-3}	2.17×10^{-3}
Modified cross-flow principle	Eq. (27)	2.08×10^{-3}	2.17×10^{-3}

SEE is the standard error of estimation, Eq. (26), while $\overline{e_c}$ in the last column is the mean of the calculated errors for each measurement, Eq. (21).

better. Assuming a friction coefficient as for a flat plate at $\mathrm{Re}_L = 1.5 \times 10^6$, and a turbulent boundary layer, gives $\pi C_F \simeq 0.012$ in Eq. (5). The coefficient $C_{n1} = 0.068$ in the linear model is based on a least-square-fit of the data for $\alpha < 4^\circ$. This value is higher than the range recommenced by Païdoussis (2004) and cannot be explained by skin friction alone. This is discussed in Thwaites (1960, Chapter IX.19–22) where the high value is explained by a secondary flow inside the boundary layer.

The cross-flow principle is found to give a better estimation than the $2D + t$ theory, again showing that the development of the flow is different in this case than in the case of an impulsively started cylinder with a laminar boundary layer.

5. Measured forces for oscillating cylinder

The results from measuring the normal force on the cylinder when running at constant speed along its axis and with harmonic oscillation in one normal direction are represented by the coefficients of the Fourier series in Eqs. (8)–(11). The coefficients for $k = 1$ and 3 are plotted in Fig. 13.

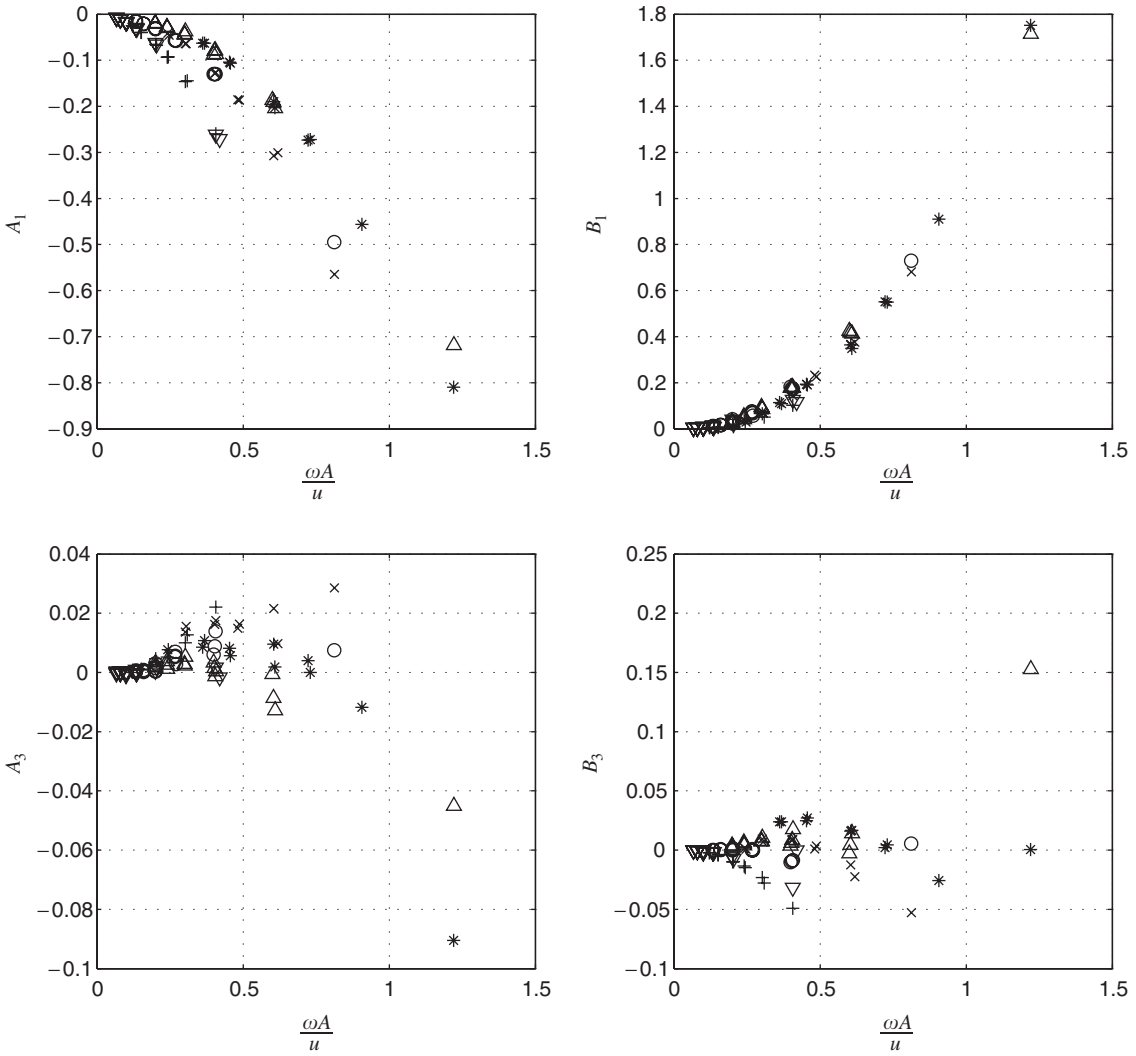

Fig. 13. Fourier series coefficients in Eqs. (8) and (9). Symbols for $L/d = 10$: +, $A/d = 1$; ×, $A/d = 2$; ∗, $A/d = 3$ and for $L/d = 30$: ▽, $A/d = 1$; ○, $A/d = 2$; △, $A/d = 3$.

The abscissa axes in Fig. 13 are the ratio between the velocity amplitude of the transverse oscillation (ωA) and the incident flow velocity along the cylinder axis u. Note that this is the tangent of the maximum angle of attack during a period of oscillation and it is therefore equivalent to the angle of attack for the constant angle case.

The error of truncating the series is illustrated in Fig. 14 where the expected relative standard error of estimation SEE_r of the Fourier series are compared with the expected error of the measurement $\overline{e_{95r}}$:

$$\overline{e_{95r}} = \frac{1}{N}\sum_{i=1}^{N}\frac{e_{95\ i}}{F_{n0\ i}}, \tag{29}$$

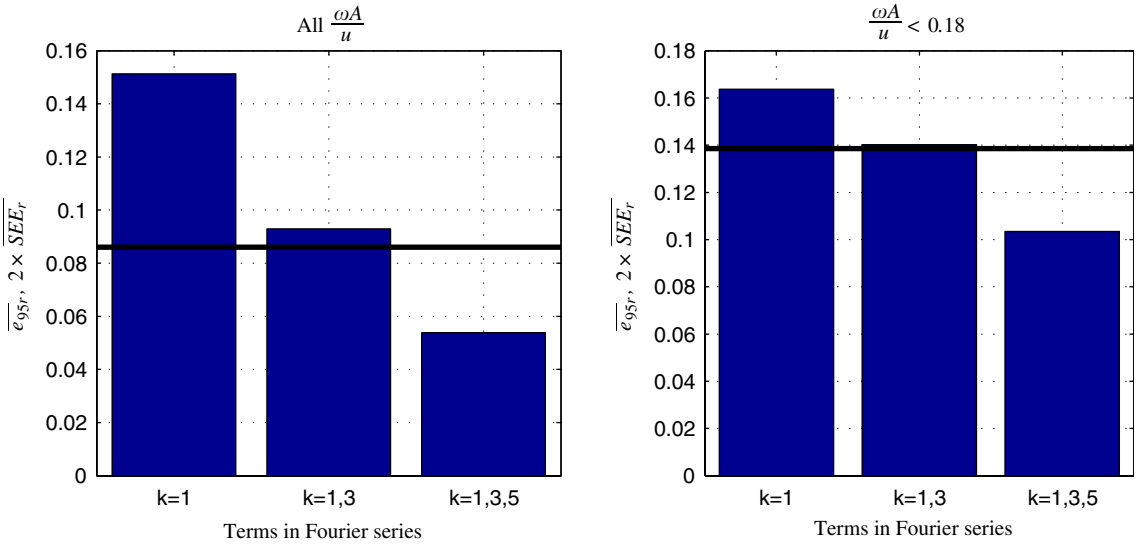

Fig. 14. Expected relative error when reproducing $D_n(\theta)$ with Fourier series. The solid line is $\overline{e_{95r}}$ (Eq. (29)), the bars are $2 \times \overline{\mathrm{SEE}_r}$ (Eq. (30)) for given terms in the Fourier series.

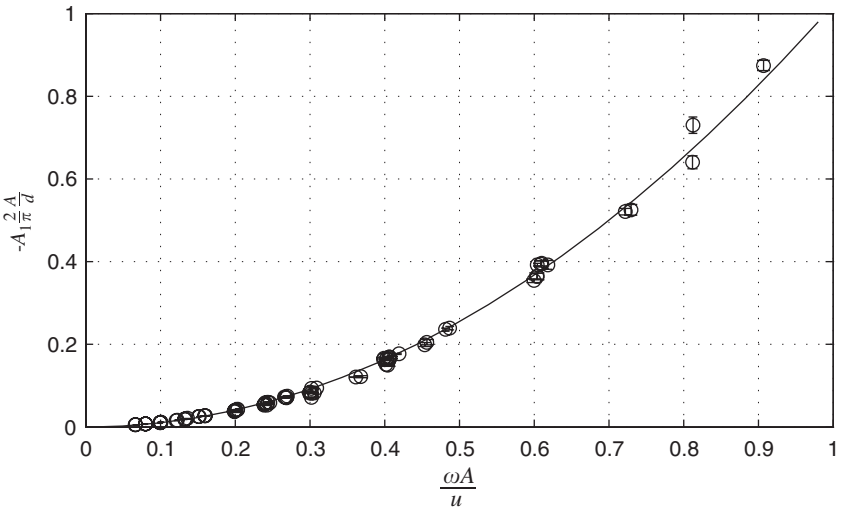

Fig. 15. Velocity amplitude ratio dependence of the added mass coefficient C_a, see also Eq. (16). All experimental results are included, and bars represents period-to-period variation of the Fourier coefficient A_1: —, $y = 1.02x^2$.

$$\mathrm{SEE}_r = \sqrt{\frac{1}{N-2}\sum_{i=1}^{N}\frac{(X_i^{\mathrm{mod}} - X_i^{\mathrm{exp}})^2}{F_{n0\ i}^2}}. \tag{30}$$

Here the index i spans N experimental values, and $F_{n0\ i}$ is the measured force amplitude for experiment i. See also Eq. (26). The estimation error is multiplied by a factor 2 in the figure to compare it with the 95% confidence interval of the measurements. The left part of the figures covers all cases in the experiment, while the right part only includes velocity ratios $\omega A/u < 0.18$. In both cases the estimation error with $k = 1$ and 3 in Eq. (8) is comparable to the experimental error, and including more terms will not give more information based on the current measurements.

The parts of Eqs. (16) and (18) not including the velocity amplitude ratio are shown in Figs. 15 and 16. These equations include only the first term in the Fourier series so the estimate in Eq. (13) cannot in general be better than about 15% of the force amplitude according to the bars for $k = 1$ in Fig. 14. This is also known from the 2-D case of an

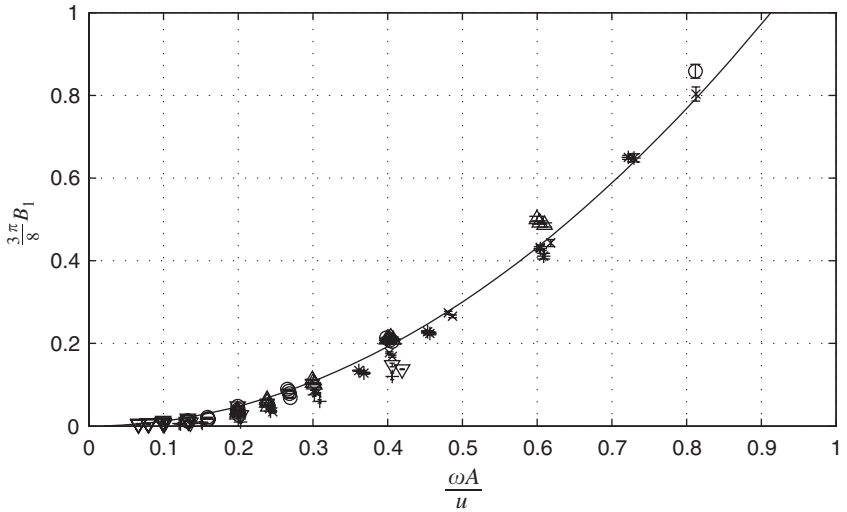

Fig. 16. Velocity amplitude ratio dependence of the drag coefficient C_d, see also Eq. (18). All experimental results are included, and bars represents period-to-period standard variation of the Fourier coefficient B_1: —, $y = 1.2x^2$.

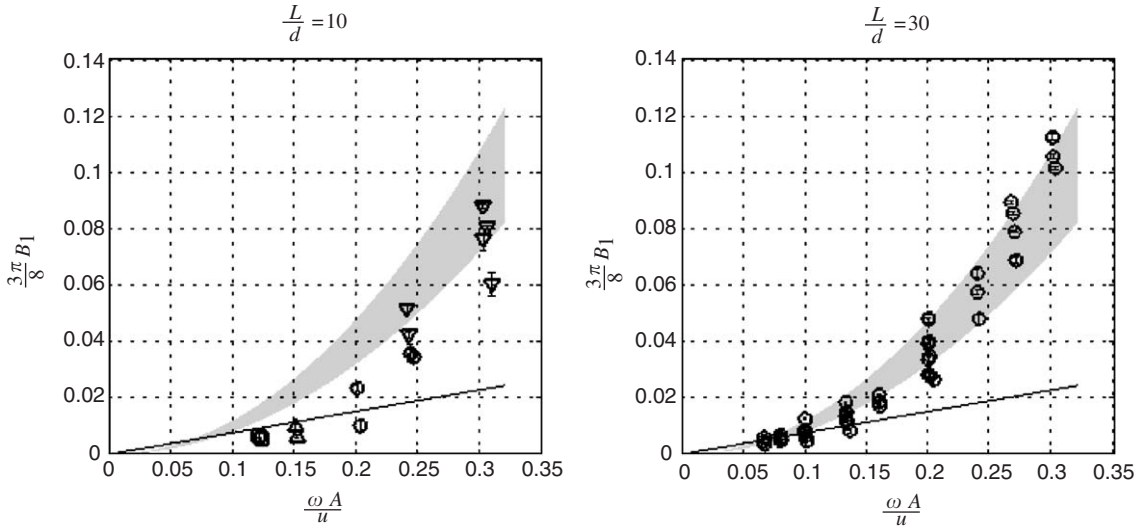

Fig. 17. Velocity amplitude ratio dependence of the drag coefficient C_d in Eq. (18) for small velocity ratios. Bars represent period to period standard variation of the Fourier coefficient B_1. Gray area corresponds to $0.8 \leqslant C_d \leqslant 1.2$; —, $y = 0.076\ x$.

oscillating cylinder section, see e.g (Sarpkaya and Isaacson, 1981). Obviously, the velocity amplitude ratio $\omega A/u$ is the dominating parameter, while the effects of parameters like length-to-diameter ratio, amplitude-to-diameter ratio and Reynolds number are of higher order. This is in contrast to the 2-D case, where the amplitude-to-diameter ratio, usually expressed by the KC number, is a dominant parameter in the range of amplitudes used in the experiment.

A least-squares-fit of the data in Fig. 15 gives

$$-\frac{2}{\pi}\frac{A}{d}A_1 = 1.02\left(\frac{\omega A}{u}\right)^2. \tag{31}$$

The standard error of estimation for this fit is 0.06 which is about three times the period-to-period variation of A_1. Inserting in Eq. (16) gives

$$C_a = 1.02, \tag{32}$$

which is very close to the theoretical result of 1.0 for inviscid flow and strip theory. The same procedure for the data in Fig. 16 and Eq. (18) gives

$$C_d = 1.2, \tag{33}$$

which is a typical asymptotic value for 2-D flow when the amplitude to diameter ratio increases.

Because the state of the boundary layer was found to be important in the stationary case, the band of silica grains were kept also for the oscillating case in order to trip the boundary layer at low angles of attack. This was to see if the variation of force due to change in the boundary layer as discussed in connection with Fig. 9 could be seen in this case also, and the result is illustrated in Fig. 17. The range of velocity amplitude ratios in these plots corresponds to angle of attacks with large Reynolds number dependent variations of the normal force in the stationary case, see Fig. 6. For small velocity ratios it was found that the L/d ratio is important, so the results for each are shown separately. Though the amplitude-to-diameter ratio was also found to have some effect, the main scatter at a given velocity ratio is a Reynolds number effect. Fig. 18 plots the measured drag coefficient against a Reynolds number defined as in Fig. 8, using the amplitude of the angle of attack. The trend is the same, but the transition seems to start at slightly lower Reynolds numbers than in the stationary case. Particularly for the smallest amplitudes, the C_d values seem to be quite low.

For the short cylinder the drag term coefficients are in general lower than for the long cylinder, indicating that some development along the cylinder as expected from the $2D + t$ principle does take place.

The lowest velocity ratio in the experiment corresponds to a maximum angle of attack of 3.7°, which is just inside the linear range in Table 3. However, because the velocity ratio corresponds to the maximum angle of attack during a cycle, the angle will be less than 4° for most of the cycle also for higher velocity ratios and a linear curve fit was therefore done

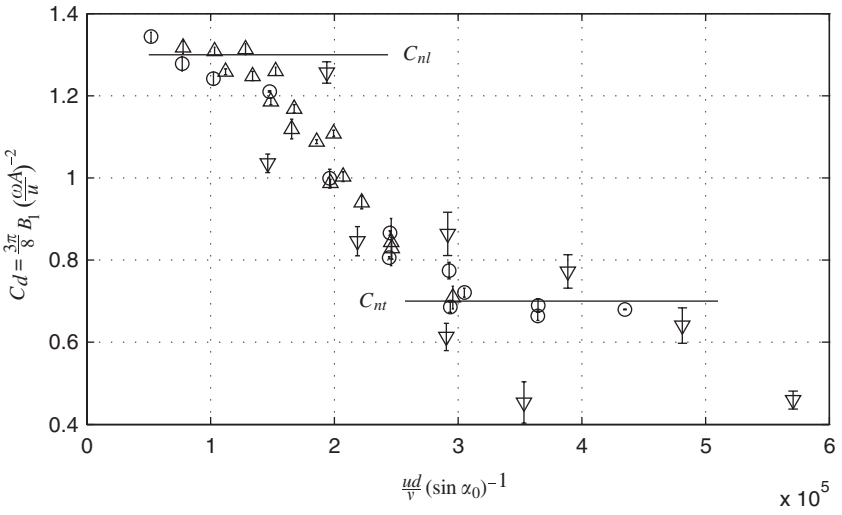

Fig. 18. Drag coefficient C_d as function of 'real' Reynolds number ($\alpha_0 = \arctan(\omega A/u)$ is the maximum angle of attack during a cycle). Bars represent period to period standard variation of the Fourier coefficient B_1. Symbols denote the oscillation amplitude: ▽, $A/d = 1$; ○, $A/d = 2$; △, $A/d = 3$. The results are for the long cylinder with $0.1 \leqslant \omega A/u \leqslant 0.4$.

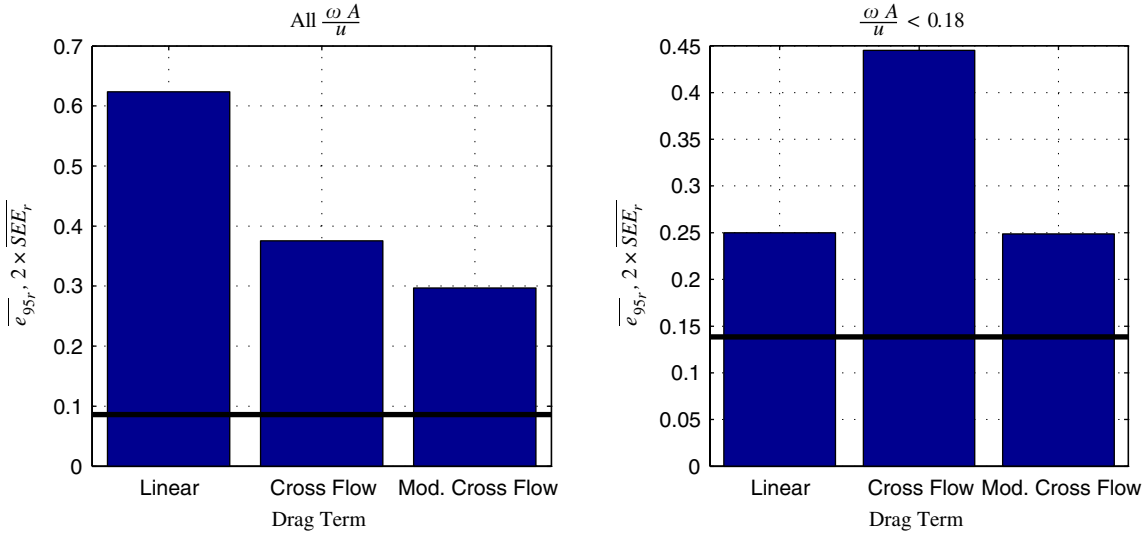

Fig. 19. Expected error when reproducing $D_n(\theta)$ with time-domain models. The solid line is $\overline{e_{95r}}$ (Eq. (29)), the bars are $2 \times \overline{\mathrm{SEE}}_r$ (Eq. (30)) for given drag term formulations.

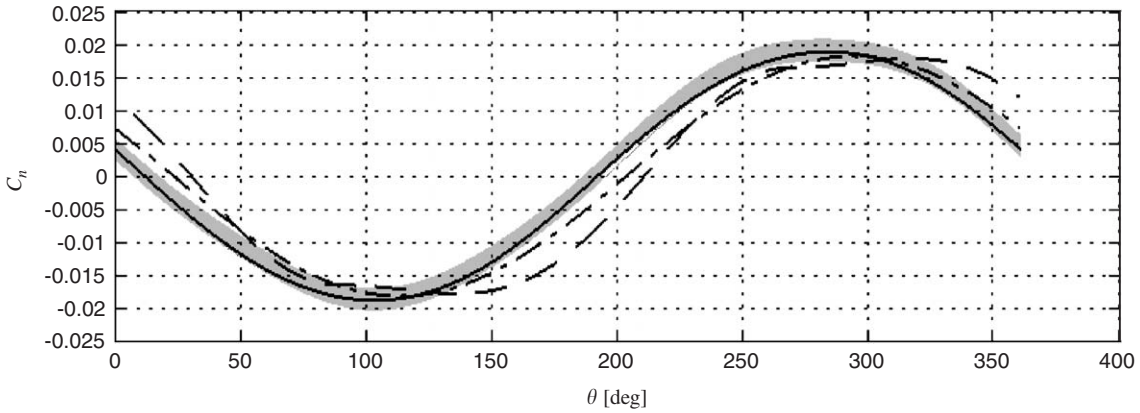

Fig. 20. Time series for $\omega A/u = 0.1$, $A/d = 1$, and $L/d = 30$: —, Fourier series with $k = 1, 3$; – –, Morison's equation; – · – Morison's equation with modified drag term. The shaded area represents the 95% confidence interval of the measurements.

for all data points with velocity ratio less or equal to 0.1. The resulting line is plotted in Fig. 17. Inserting this in Eq. (19) and realizing that $\cos\alpha \simeq 1$ for small α gives a linear model of the damping. The value of the coefficient was found to be

$$C_{n1} = 0.076, \tag{34}$$

which is comparable to the value found in the stationary case, see Table 3.

6. Time-domain models of the oscillating force

The Fourier series formulation above was successful in reproducing the experimental results, but in a general time-domain simulation the motion of a body is not harmonic and the forces cannot be described this way. In the general case it would be preferable if only the instantaneous accelerations, velocities and the orientation of the body were included in the force model. Due to the low scatter of Fig. 15 it will be assumed that the inertia part can be

modelled as in Eq. (12), with coefficient from Eq. (32). Possible expressions for the drag term are the linear form in Table 3 with coefficient from Eq. (34) or the cross-flow term in Table 3 with coefficient from Eq. (33). In addition, an attempt is made to formulate a model based on the discussion above. This is the same as the modified cross-flow model in Eqs. (27) and (28) but the limits for the real Reynolds number are set to $Ud/\nu(\sin\alpha_t)^{-1} = 3.0 \times 10^5$ and $Ud/\nu(\sin\alpha_l)^{-1} = 1.5 \times 10^5$ according to Fig. 18. The coefficients for laminar and turbulent flow are $C_{nl} = 1.3$ and $C_{nt} = 0.7$, respectively, indicated by lines in Fig. 18. In addition, values for instantaneous angles of attack less than 6° are replaced with the linear model. The expected errors, defined as twice the standard error of estimation, are shown in Fig. 19.

The error levels are quite high, but the modified model does improve the performance. This is again taken as an indication that the shift in boundary layer seen in the stationary case also does take place in the oscillating case. It also seems that a linear model is the better choice for small angles.

Selected time histories are shown in Figs. 20–22. Note that the measured time histories do not show the shape associated with a quadratic drag term even for high velocity amplitude ratios. This is even true for $A/d = 3$ where the drag term is dominant. That the drag, or velocity-dependent, term dominates here is indicated by the fact that the phase angle of the force peaks is close to the phase angle of the maximum velocity ($\theta = 180°$ and 360°). The absence of a

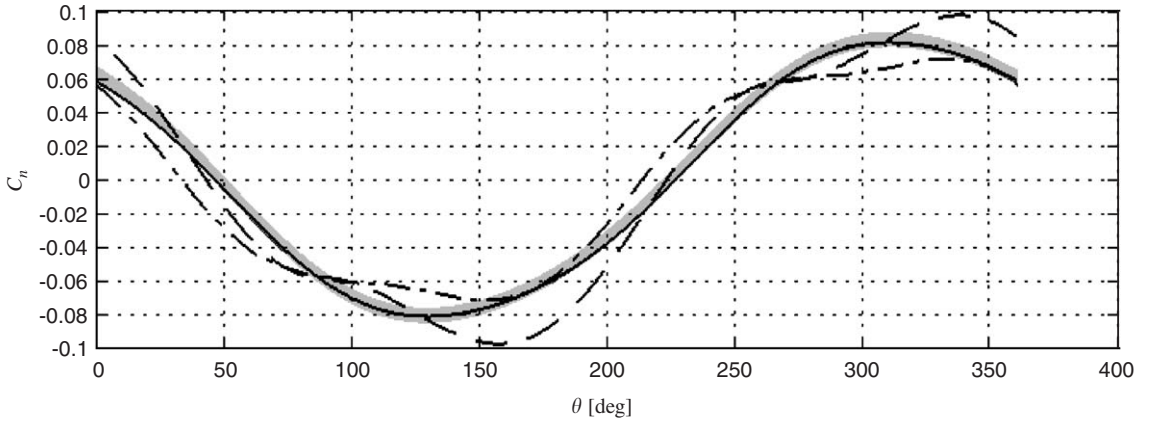

Fig. 21. Time series for $\omega A/u = 0.27$, $A/d = 2$, and $L/d = 30$: —, Fourier series with $k = 1, 3$; – –, Morison's equation; – · –, Morison's equation with modified drag term. The shaded area represents the 95% confidence interval of the measurements.

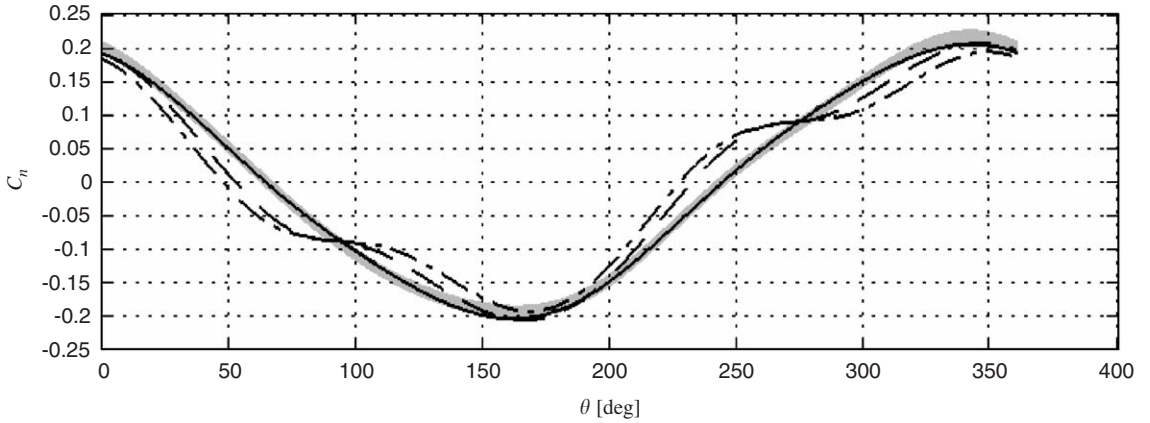

Fig. 22. Time series for $\omega A/u = 0.4$, $A/d = 3$, and $L/d = 30$: —, Fourier series with $k = 1, 3$; – –, Morison's equation; – · –, Morison's equation with modified drag term. The shaded area represents the 95% confidence interval of the measurements.

quadratic drag term then seems to be the main reason for the poor results in Fig. 19, and it is particularly bad for $A/d = 2$ where the inertia and drag terms are of comparable magnitude.

7. Conclusion

From the discussion in the foregoing it is clear that the axial flow does influence the normal force on a cylinder for low angles of attack. The important parameters in the stationary case are the angle of attack and a Reynolds number based on the length of the cylinder parallel to the incoming flow. In the oscillating case, the amplitudes of these parameters were used to show a similar dependence. Other parameters like length-to-diameter ratio and amplitude-to-diameter ratio of the oscillation are found to be of lesser importance than expected a priori.

If the angle of attack is less than about 4°–5°, the normal force is linear with the normal velocity component of the ambient flow, similar to the equation of lift on an airfoil section. This seems to be the case both for a steady and an oscillating angle of attack. The coefficient is too high to be accredited to skin friction alone.

For angles larger than 5°, the cross-flow principle can be applied if the state of the boundary layer is taken into account. A 'real' Reynolds number can be defined based on the instantaneous length of the body parallel to the incident flow. The normal force coefficient plotted against this Reynolds number looks very similar to the drag coefficient of a 2-D cylinder plotted against the Reynolds number based on the diameter. This means that there is a sub-critical region, a transition region and a super-critical region where the drag coefficient is lower than in the sub-critical flow domain.

For the oscillating case the main parameter seems to be the ratio of transverse velocity amplitude to the axial velocity, or the maximum angle of attack. The amplitude to diameter ratio is also a parameter, but the importance is found to be less than expected from the 2-D case.

Also the length-to-diameter ratio was found to be of less importance than a 2D + t theory might suggest, at least for the stationary case. In the oscillating case the force term seemed to be smaller for the short cylinder than for the long one, particularly at small angles.

In simulating slender marine systems with a high axial component a model based on the angle of attack and the absolute value of the relative velocity between body and fluid as in Eq. (27) seems to be the best choice. For the oscillating case, the errors in the estimated force might be quite high, the expected standard error of estimation for the best model discussed here is about 15% of the force amplitude.

The current study only includes the normal component of the force. Because asymmetric vortex separation associated with the cross-flow principle certainly takes place, it is expected that a bi-normal force is also present. Also, the present study assumes a smooth cylinder, thus the effect of roughness or something like a stranded wire is not considered, and might be a topic for further studies. Another topic for further studies is to apply and verify the current results in calculating the dynamic response of a flexible cylinder where the modelling of the damping may be crucial.

Acknowledgment

This work is part of a Strategic University Program in Marine Cybernetics, founded by the Norwegian Research Council. Funding is also received from the Strategic University Program in Hydroelasticity and the Centre of Ship and Offshore Structures, both at NTNU.

References

Blevins, R.D., 1992. Applied Fluid Dynamics Handbook. Krieger Publishing Company, Malabar, FL.

Bryson, A., 1959. Symmetric vortex separation on circular cylinders and cones. Journal of Applied Mechanics, pp. 643–648.

Coleman, H., Steele, W., 1989. Experimentation and Uncertainty Analysis for Engineers. Wiley, New York.

Dowling, A.P., 1988. The dynamics of flexible slender cylinders. Part 1: neutrally buoyant elements. Journal of Fluid Mechanics 187, 507–533.

Ersdal, S., 2004. An experimental study of hydrodynamic forces on cylinders and cables in near axial flow. Ph.D. Thesis, Norwegian University of Science and Technology.

Faltinsen, O.M., 1990. Sea Loads on Ships and Offshore Structures. Cambridge University Press, Cambridge.

Faltinsen, O.M., 2005. Hydrodynamics of High-Speed Marine Vehicles. Cambridge University Press, New York.

Hoerner, S., Borst, H., 1985. Fluid-Dynamic Lift. Liselotte A. Hoerner, Brick Town, NJ.

ITTC, 1990. Report of the Panel on Validation Procedures. 19th International Towing Tank Conference, Madrid, Spain.

Jorgensen, L., Perkins, E., 1958. Investigation of some wake vortex characteristics of an inclined ogive cylinder body at Mach number 2. Report 1371, NACA.

Keulegan, H., Carpenter, H., 1958. Forces on cylinders and plates in an oscillating fluid. Journal of Research of the National Bureau of Standards 60 (5) 423–440.

Koumoutsakos, P., Leonard, A., 1995. High-resolution simulations of the flow around an impulsively started cylinder using vortex methods. Journal of Fluid Mechanics 296, 1–38.

Lighthill, M., 1960. Note on the swimming of slender fish. Journal of Fluid Mechanics 9, 305–317.

Newman, J., 1977. Marine Hydrodynamics. MIT Press, Cambridge, MA.

Païdoussis, M., 2004. Fluid-Stucture Interactions, vol. 2: Slender Structures and Axial Flow. Elsevier Academic Press, San Diego.

Sarpkaya, T., 1966. Separated flow about lifting bodies and impulsive flow about cylinders. AIAA Journal, 414–420.

Sarpkaya, T., Isaacson, M., 1981. Mechanics of Wave Forces on Offshore Structures. Van Nostrand, Reinhold, New York.

Schlichting, H., 1979. Boundary-Layer Theory, seventh ed. McGraw-Hill, New York.

Taylor, G., 1952. Analysis of the swimming of long and narrow animals. Proceedings of the Royal Society of London 214, 158–183.

Thwaites, B., 1960. Incompressible Aerodynamics. Clarendon Press, Oxford.

Triantafyllou, G., Chryssostomidis, C., 1988. The dynamics of towed arrays. In: Proceedings of the Seventh International Offshore Mechanics and Arctic Engineering Symposium, ASME, New York, pp. 383–389.

White, F., 1972. An analysis of axisymmetric turbulent flow past a long cylinder. ASME Journal of Basic Engineering 94, 200–206.